PHYSICAL REVIEW C, VOLUME 62, 025202

Deeply bound π^- states in ^{207}Pb formed in the ^{208}Pb$(d,^3$He$)$ reaction. II. Deduced binding energies and widths and the pion-nucleus interaction

K. Itahashi,* K. Oyama, and R. S. Hayano
Department of Physics, University of Tokyo, 7-3-1 Hongo, Bunkyo-ku, Tokyo 113, Japan

H. Gilg, A. Gillitzer, M. Knülle, M. Münch, W. Schott, and P. Kienle
Physik-Department, Technische Universität München, D-85747 Garching, Germany

H. Geissel, N. Iwasa, and G. Münzenberg
Gesellschaft für Schwerionenforschung, D-64291 Darmstadt, Germany

S. Hirenzaki
Department of Physics, Nara Women's University, Nara 630, Japan

H. Toki
Research Center for Nuclear Physics, Osaka University, Osaka 567, Japan

T. Yamazaki
Institute of Particle and Nuclear Studies, High Energy Accelerator Research Organization, 3-2-1 Midori-cho, Tanashi, Tokyo 188-8501, Japan
and Japan Society for the Promotion of Science, 5-3-1 Koji-machi, Chiyoda-ku, Tokyo 102-0083, Japan

(Received 28 July 1999; revised manuscript received 18 April 2000; published 13 July 2000)

We find a remarkable agreement of the excitation energy spectrum of the ^{208}Pb$(d,^3$He$)$ reaction measured at $T_d=600$ MeV near the π^- production threshold with its theoretical prediction. Their comparison leads us to assign the distinct narrow peak observed at about 5 MeV below the threshold to the formation of bound pionic states $\pi^-\otimes^{207}$Pb of the quasisubstitutional configurations $(2p)_{\pi^-}(3p_{3/2},3p_{1/2})_n^{-1}$. A small bump observed on the tail of the peak is assigned to the pionic $1s$ state. The binding energies (B_{nl}) and the widths (Γ_{nl}) of the pionic orbitals are deduced to be $B_{2p}=5.13\pm0.02$ (stat) ±0.12 (syst) MeV and $\Gamma_{2p}=0.43\pm0.06$ (stat) ±0.06 (syst) MeV by decomposing the experimental spectrum into the pionic $1s$ and $2p$ components. While B_{2p} and Γ_{2p} are determined with small ambiguity, B_{1s} and Γ_{1s} are strongly correlated with each other, and are affected by the relative $1s/2p$ cross section ratio assumed, since the $1s$ component is observed only as an unresolved bump. Thus, we have to allow large uncertainties $6.6\,\text{MeV}<B_{1s}<6.9\,\text{MeV}$ and $0.4\,\text{MeV}<\Gamma_{1s}<1.2$ MeV. The experimental binding energies and widths are compared with theoretically calculated values based on various optical potential parameter sets, and are jointly used to deduce the effective π^- mass in the nuclear medium.

PACS number(s): 36.10.Gv, 14.40.Aq, 25.45.Hi, 27.80.+w

I. INTRODUCTION

As described in the preceding paper [1], we performed a high-resolution measurement of the nuclear excitation spectrum near the pion production threshold in the ^{208}Pb$(d,^3$He$)$ reaction measured at incident deuteron energy of 600 MeV. This experiment was based on the theoretical prediction for the population of deeply bound pionic states [2–4] by using pion-transfer reactions [5,6]. We observed a distinct narrow peak around an excitation energy of 135 MeV, about 5 MeV below the π^- production threshold. The peak was assigned to the formation of bound pionic states of $\pi^-\otimes^{207}$Pb with the quasisubstitutional configurations $(2p)_{\pi^-}(3p_{3/2},3p_{1/2})_n^{-1}$. An additional bump was observed at about 6.5 MeV below the threshold which corresponds to the $(1s)_{\pi^-}$ component. A short description of the first results was published [7] and their implications in terms of the pion effective mass were given elsewhere [8]. In the present paper we analyze the excitation spectrum presented in the preceding paper in details in order to deduce the binding energies and the widths of the bound pionic orbitals (Sec. II), to compare the deduced values to the theoretical prediction (Sec. III), and to relate them to the pion-nucleus interaction (Sec. IV). A brief history of deeply bound pionic atom exploration and possible future perspective are found in Sec. V.

II. DEDUCTION OF THE BINDING ENERGIES AND THE WIDTHS

A. The excitation spectrum and configuration assignment

The ^{208}Pb$(d,^3$He$)\pi^-\otimes^{207}$Pb is a nucleon-pickup type reaction with a π^- transfer and its elementary process is $n(d,^3\text{He})\pi^-$. The produced bound π^- states have configu-

*Electronic address: itahashi@phys.s.u-tokyo.ac.jp

TABLE I. Neutron hole excitation energies of ^{207}Pb(E_n), and the spectroscopic strengths $[C^2S/(2j'+1)]$ obtained by (p,d) reactions [18]. Expected excitation energies referred to the ground state of ^{207}Pb for the configurations of $(nl)_{\pi^-}(n'l'j')_n^{-1}$ and the effective neutron numbers $(N_{\rm eff})$ for the ^{208}Pd$(d,^3$He) reaction at the incident beam energy of 600 MeV using the SM-1 parameter set.

	$n'l'_{j'}$	$3p_{1/2}$	$2f_{5/2}$	$3p_{3/2}$	$1i_{13/2}$	$2f_{7/2}$	$1h_{9/2}$	$1h_{11/2}$
E_n [MeV]		$g.s.=0.0$	0.570	0.900	1.63	2.34	3.41	9.17
$C^2S/(2j'+1)$		1.00	0.90	0.89	0.56	0.56	0.55	-
E_x [MeV]	$1s_\pi$	132.61	133.18	133.51	134.24	134.95	136.02	141.78
	$2p_\pi$	134.41	132.98	135.31	136.04	136.75	137.82	143.58
$N_{\rm eff}$	$1s_\pi$	1.63×10^{-3}	2.15×10^{-3}	2.46×10^{-3}	1.21×10^{-4}	1.33×10^{-3}	0.95×10^{-4}	1.97×10^{-4}
	$2p_\pi$	7.58×10^{-3}	4.18×10^{-3}	1.26×10^{-2}	3.46×10^{-4}	2.80×10^{-3}	1.99×10^{-4}	4.63×10^{-4}

rations $(nl)_{\pi^-}(n'l'j')_n^{-1}$ and for each state the excitation energy (E_x) with respect to the ground state of ^{207}Pb is related to the pion binding energy (B_{nl}) as

$$E_x=[M_x-M(^{207}\mathrm{Pb})]c^2=m_{\pi^-}c^2-B_{nl}+E_n(n'l'j'),$$

where M_x is the mass of the reaction product, $m_{\pi^-}=139.57\,\mathrm{MeV}/c^2$ is the pion mass and $E_n(n'l'j')$ is the excitation energy of ^{207}Pb, as presented in Table I.

Figure 1 (upper) shows the measured excitation spectrum of the ^{208}Pb$(d,^3$He) reaction near the threshold. The abscissa is the excitation energy and the ordinate is the double differential cross section. A monoenergetic peak of ^{3}He produced in the $p(d,^3\mathrm{He})\pi^0$ reaction on a $(CH_2)_n$ target is overlaid in the excitation energy scale so as to demonstrate the symmetrical shape of the overall resolution function. This peak was also used as an absolute calibration of the excitation energy. Note that the instrumental width is much larger for the $(CH_2)_n$ target than for the ^{208}Pb target due to the different target thickness [1].

The spectrum stands on a structureless background of about 5 μb/(MeV sr) which extends towards the region $E_x<132$ MeV. On the right-hand side of the π^- emission threshold, there is a quasifree pion production continuum. Between 137 and 139 MeV one notices several small peaks due to the production of shallowly bound pionic states of $3p$,$3d$,$4p$,..., some of which had been known from pionic x-ray spectroscopy [9,10]. A prominent peak is seen around $E_x=135$ MeV, which is about 5 MeV below the π^- emission threshold. A small shoulderlike structure can also be seen around $E_x=134$ MeV. Comparing the shape to the theoretically calculated spectrum shown in Fig. 1 (lower), we can assign the peak and the shoulder to the configurations of $(2p)_{\pi^-}(3p_{3/2})_n^{-1}$ and $(2p)_{\pi^-}(3p_{1/2})_n^{-1}$, respectively. The experimental shape agrees with the theoretical one with the expected intensity ratio of 2:1 and the energy difference of 0.9 MeV of the two main configurations. While the pionic $2p$ component is clearly seen as a composite peak, the $1s$ component is observed only as a small bump around $E_x=133$ MeV. The major configurations which contribute to the $1s$ bump are $(1s)_{\pi^-}(3p_{1/2})_n^{-1}$, $(1s)_{\pi^-}(2f_{5/2})_n^{-1}$, and $(1s)_{\pi^-}(3p_{3/2})_n^{-1}$ as shown in Fig. 2 (lower).

B. Theoretical spectral shape

1. Pion-nucleus optical potential

In order to obtain the theoretically calculated spectrum as shown in Fig. 1 (lower), we took the following approach. We solved the Klein-Gordon equation

$$[-\nabla^2+\mu^2+2\mu U_{\rm opt}(r)]\phi(r)=[E-V_c(r)]^2\phi(r), \tag{2.1}$$

where μ is the pion-nucleus reduced mass and $V_c(r)$ is the Coulomb potential with finite size charge distribution

$$V_c(r)=-e^2\int\frac{\rho^{(p)}(r')}{|\mathbf{r}-\mathbf{r}'|}d^3r', \tag{2.2}$$

with $\rho^{(p)}(r')$ being the proton density distribution. For the nucleon density distribution in ^{207}Pb, we used the two-parameter Fermi model

$$\rho(r)=\frac{\rho(0)}{1+\exp[(r-c)/z]} \tag{2.3}$$

with

$$c=6.62\ \ \mathrm{fm}$$

$$z=0.546\ \ \mathrm{fm}$$

for both the proton $[\rho^{(p)}(r)]$ and the neutron $[\rho^{(n)}(r)]$ [11], and

$$\rho^{(p)}(0)=0.0632\ \ \mathrm{fm}^{-3}=0.179\,m_\pi^3,$$

$$\rho^{(n)}(0)=0.0964\ \ \mathrm{fm}^{-3}=0.272\,m_\pi^3,$$

$$\rho^{(0)}=0.1596\ \ \mathrm{fm}^{-3}=0.451\,m_\pi^3,$$

$$\Delta\rho(0)=0.0332\ \ \mathrm{fm}^{-3}=0.0938\,m_\pi^3.$$

For the strong interaction optical potential $U_{\rm opt}(r)$ [12,13], we employed the expression given by Ericson and Ericson [13]

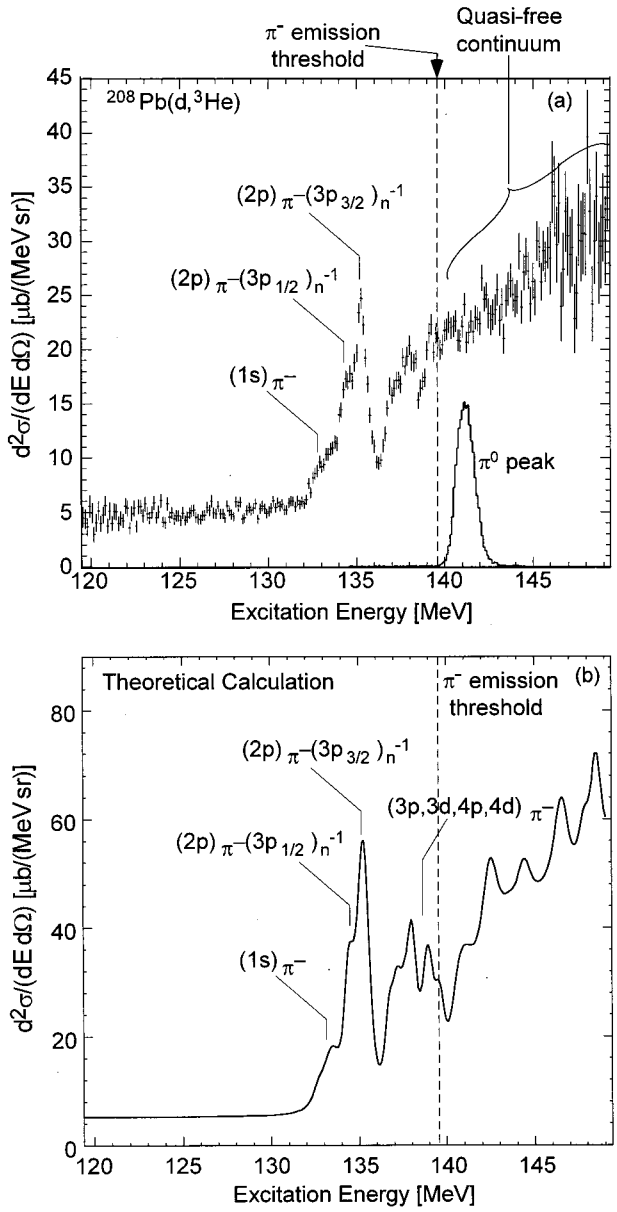

FIG. 1. (a) The excitation spectrum in the reaction ^{208}Pb$(d,^3$He$)$ at $T_d=600$ MeV. The prominent peak around the excitation energy of 135.4 MeV is assigned to the configuration of $(2p)_{\pi^-}(3p_{3/2})_n^{-1}$, and its satellite to $(2p)_{\pi^-}(3p_{1/2})_n^{-1}$. The small bump seen around 133 MeV is due to the production of the $1s$ pionic state. The monoenergetic peak from the $p(d,^3\mathrm{He})\pi^0$ reaction used as a calibration is also shown. (b) A theoretically calculated excitation spectrum of the ^{208}Pb$(d,^3$He$)$ reaction at $T_d=600$ MeV. We considered 16 neutron hole states (both for bound and quasi-free π^- contribution) and 10 proton hole states (for quasi-free π^0 contributions) in the calculation. A constant background of 5 μb/(MeV sr) and an experimental resolution of 0.48 MeV FWHM are assumed.

$$2\mu U_{\mathrm{opt}}(r) = -4\pi[b(r)+\epsilon_2 B_0\rho^2(r)] + 4\pi\nabla[c(r) + \epsilon_2^{-1}\{C_0\rho^2(r)+C_1\Delta\rho(r)\rho(r)\}]L(r)\nabla, \tag{2.4}$$

with

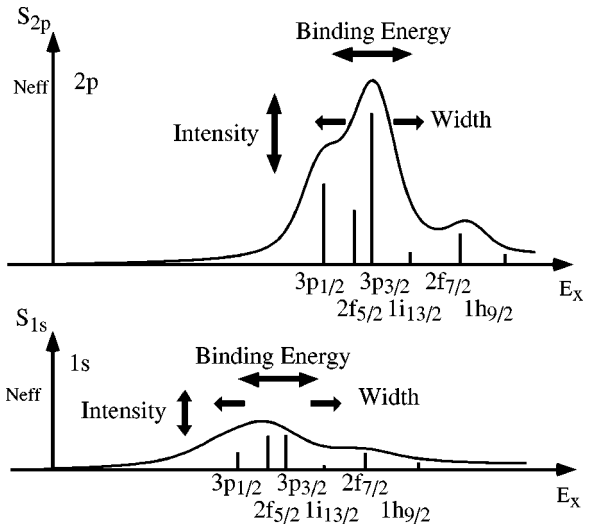

FIG. 2. Calculated spectral shapes of the pionic $2p$ (upper) and the $1s$ (lower) components. The solid curves show the shapes of the components. The vertical lines show the positions and the sizes of the Lorentzian peaks corresponding to configurations $(nl)_{\pi^-}(n'l'j')_n^{-1}$.

$$b(r)=\epsilon_1\{b_0\rho(r)+b_1\Delta\rho(r)\},$$

$$c(r)=\epsilon_1^{-1}\{c_0\rho(r)+c_1\Delta\rho(r)\},$$

$$L(r)=\left[1+\frac{4}{3}\pi\lambda[c(r)+\epsilon_2^{-1}\{C_0\rho^2(r) + C_1\Delta\rho(r)\rho(r)\}]\right]^{-1},$$

$$\rho(r)=\rho^{(n)}(r)+\rho^{(p)}(r),$$

$$\Delta\rho(r)=\rho^{(n)}(r)-\rho^{(p)}(r),$$

where $\epsilon_1=1+\mu/M=1.147$, $\epsilon_2=1+\mu/2M=1.073$ with M being the nucleon mass. The λ denotes the Lorentz-Lorenz correction parameter. $b(r)$ and B_0 are the parameters for the local (s-wave) part and $c(r)$, C_0, and C_1 are for the nonlocal (p-wave) part. $b(r)$ and $c(r)$ are real and the others are complex.

There are several parameter sets based on the existing pionic atom data. We list them in Table II together with the calculated $1s$ and $2p$ binding energies and widths. In the calculation of the spectrum shown in Fig. 1 (lower) and for the peak decomposition described in the next section, we took the SM-1 parameter set.

2. Effective number approach

We calculated the formation cross sections of bound pionic states in the ^{208}Pb$(d,^3$He$)$ reaction by an effective number approach [6,14]. The treatment of the quasifree production is discussed in detail in Ref. [15]. Using the cross section of the $nd\rightarrow{}^3\mathrm{He}\pi^-$ reaction at forward angles, the formation cross section is expressed as

TABLE II. Several parameter sets of Ericson-Ericson optical potential and calculated binding energies and widths of pionic $1s$ and $2p$ states in ^{207}Pb. For Konijn-1-5 and Nieves, the binding energies and the widths were taken from their references and were for $\pi^- \otimes {}^{208}$Pb. The difference of the isotopes does not cause serious deviations. The parameters of Konijn-3-5 and Nieves are not shown because the standard Ericson-Ericson formulation was not used in these calculations. For Batty-3, the density parameters used in the calculation were $c=6.654$ fm and $a=0.475$ fm for the proton and $c=6.900$ fm and $a=0.475$ fm for the neutron. In the calculations of Ericson-1-3, we applied the Pauli correlations in Refs. [57,58] with the Fermi momentum of 265 MeV/c from Ref. [59], approximated k^2 in Ref. [27] to $-2\mu V_c(r)$ and neglected $O(1/A)$ terms. In Ericson-2 and -3, finite range correction is included.

	Ref.	λ	b_0 (m_π^{-1})	b_1 (m_π^{-1})	c_0 (m_π^{-3})	c_1 (m_π^{-3})	Re B_0 (m_π^{-4})	Im B_0	Re C_0 (m_π^{-6})	Im C_0	Re C_1 (m_π^{-6})	Im C_1	B_{1s} MeV	Γ_{1s} MeV	B_{2p} MeV	Γ_{2p} MeV
Tauscher	[22]	1	−0.0293	−0.078	0.227	0.18	0	0.0428	0	0.076	0	0	7.022	0.687	5.212	0.462
Batty-1	[24]	1	−0.017	−0.13	0.255	0.17	−0.0475	0.0475	0	0.09	0	0	6849	0.602	5.128	0.353
Batty-2	[25]	1	−0.023	−0.085	0.21	0.089	−0.021	0.049	0.118	0.058	0	0	7.021	0.697	5.209	0.742
Batty-3	[23]	0	0	−0.125	0.261	0.104	−0.14	0.055	−0.25	0.059	0	0	6.604	0.537	4.996	0.292
SM-1	[26]	1	−0.0283	−0.12	0.223	0.25	0	0.042	0	0.1	0	0	6.870	0.582	5.130	0.374
SM-2	[26]	1	0.03	−0.143	0.21	0.18	−0.15	0.046	0.11	0.09	0	0	7.308	0.850	5.388	0.550
Konijn-1	[28]	0	0.024	−0.090	0.272	0.107	−0.261	0.0552	−0.26	0.0640	0	0	6.785	0.475	5.082	0.322
Konijn-2	[28]	1	0.025	−0.094	0.273	0.184	−0.265	0.0546	−0.14	0.105	0	0	6.777	0.458	5.079	0.312
Konijn-3	[28]												6.924	0.063	5.138	0.154
Konijn-4	[28]												6.897	0.089	5.133	0.156
Konijn-5	[28]												6.932	0.118	5.143	0.159
Nieves	[29]												6.778	0.409	5.105	0.275
Ericson-1	[27]	1	−0.0192	−0.0873	0.2087	0.1779	−0.0489	0.0489	0.1988	0.0879	−0.737	0	6.932	0.685	5.155	0.413
Ericson-2	[27]	1	−0.0192	−0.0873	0.2087	0.1779	−0.0489	0.0489	0.1988	0.0879	−0.737	0	6.709	0.557	5.035	0.292
Ericson-3	[27]	1	−0.0178	−0.0873	0.2087	0.1779	−0.0489	0.0489	0.1988	0.0879	−0.737	0	6.735	0.571	5.050	0.304

$$\left[\frac{d\sigma}{d\Omega}\right]_{dA\to{}^3\mathrm{He}(A-1)\pi} = \left[\frac{d\sigma}{d\Omega}\right]_{dn\to{}^3\mathrm{He}\pi} \times N_{\mathrm{eff}}. \tag{2.5}$$

The effective neutron number (N_{eff}) is described as

$$N_{\mathrm{eff}} = \sum_{M,m_s} \left| \int \chi_f^*(\mathbf{r})\xi^*_{1/2,m_s}(\sigma)[\phi_l^*(\mathbf{r}) \otimes \psi_{j'}(\mathbf{r},\sigma)]_{JM}\chi_i(\mathbf{r})d^3r\,d\sigma \right|^2 \times C^2S/(2j'+1), \tag{2.6}$$

where $\phi_l(\mathbf{r})$ and $\psi_{j'}(\mathbf{r},\sigma)$ are the wave functions of the bound pion and the neutron hole, respectively, with a resultant angular momentum J. The neutron wave functions were obtained by using a Woods-Saxon type potential, and the pion wave functions by solving the Klein-Gordon equation [Eq. (2.1)]. The spin wave function $\xi_{1/2,m_s}(\sigma)$ reflects the possible spin directions of the neutrons. χ_i and χ_f denote the initial and the final distorted waves of the projectile and the ejectile, respectively. We used the eikonal approximation

$$\chi_f^*(\mathbf{r})\chi_i(\mathbf{r}) = \exp(i\mathbf{q}\cdot\mathbf{r})D(\mathbf{b},z) \tag{2.7}$$

with a distortion factor

$$D(\mathbf{b},z) = \exp\left[-\frac{1}{2}\left(\int_{-\infty}^{z}\sigma_d\rho(\mathbf{b},z')dz' + \int_z^{\infty}\sigma_{{}^3\mathrm{He}}\rho(\mathbf{b},z')dz'\right)\right], \tag{2.8}$$

where σ_d is the deuteron-nucleon total cross section, $\sigma_{{}^3\mathrm{He}}$ is the ^{3}He-nucleon cross section derived from Ref. [16], z is the coordinate of the reaction point along the beam direction and $\rho(\mathbf{b},z')$ is the density distribution of the nucleus at impact parameter $\mathbf{b}$ and beam coordinate z'.

In this formula, we have introduced several corrections compared to the one shown in Ref. [7]. The previous results used the elementary pion production cross section $\sigma(n+d \to {}^3\mathrm{He}+\pi^-)$ at zero degree in the laboratory frame $\sigma(0°) = 3.7$ mb/sr. This value was obtained by using the angular distribution of $p+d$ reactions at 325 MeV/nucleon from existing data. In the new calculation used here, an elementary cross section $\sigma(0°) = 2.8$ mb/sr was used. This value was derived by an extrapolation from the experimental data of $d+p\to t+\pi^+$ cross sections into this energy range ($T_d = 300-800$ MeV) [5] based on the theoretical work of Fearing [17] on the energy dependence of the reaction. The erroneous inclusion of a factor $\frac{1}{2}$ in the effective number due to a double counting of the spin degeneracy was also corrected. In addition, the neutron hole spectroscopic factors shown in Table I [$C^2S/(2j'+1)$] were used to take the neutron state fragmentation [18] into consideration as shown in Eq. (2.6). The obtained effective numbers for major configurations are listed together in Table I. In the calculated spectrum shown in Fig. 1 (lower) we took 16 neutron holes into account and assumed a constant background of 5 μb/(MeV sr) and an instrumental resolution of 0.48 MeV. The peaks seen on the quasifree continuum are due to the fact that the unknown widths of deep neutron hole states were assumed to be 0 MeV.

C. Deduction of B_{nl} and Γ_{nl} by spectral decomposition

So far, we have used the theoretical spectrum shown in Fig. 1 (lower) as a guide to assign the configurations to the experimental spectrum. Now, in order to precisely determine the binding energies (B_{nl}) and the widths (Γ_{nl}) of the pionic $1s$ and the $2p$ states, we fit the excitation spectrum with a sum of a background and the contributions from the two pionic orbitals ($1s$ and $2p$ as shown in Fig. 2). We set the fitting region to be between 120.0 MeV and 136.0 MeV in order to avoid contributions from the tails of shallowly bound states. The lowest six neutron hole states which have considerable contributions in the fitting region, $3p_{1/2}$, $2f_{5/2}$, $3p_{3/2}$, $1i_{13/2}$, $2f_{7/2}$, and $1h_{9/2}$, are taken into account in the fitting procedure. See Table I for the properties of the neutron hole states.

The fitting function comprises the pionic $1s$ component, the $2p$ component and a linear background as

$$S(E_x)=S_{1s}(E_x;I_{1s},B_{1s},\Gamma_{1s})+S_{2p}(E_x;I_{2p},B_{2p},\Gamma_{2p}) + S_{bg}(E_x;c_0,c_1), \tag{2.9}$$

where

$$S_{1s}=I_{1s}\times\sum_{n'l'j'}N_{\rm eff}(1s,n'l'j') \times F[(E_x;m_\pi-B_{1s}+E_n(n'l'j'),\Gamma_{1s},\sigma_{\rm exp})] \tag{2.10}$$

$$S_{2p}=I_{2p}\times\sum_{n'l'j'}N_{\rm eff}(2p,n'l'j') \times F[E_x;m_\pi-B_{2p}+E_n(n'l'j'),\Gamma_{2p},\sigma_{\rm exp}] \tag{2.11}$$

$$S_{bg}=c_0+c_1\times E_x. \tag{2.12}$$

Here, $N_{\rm eff}(nl,n'l'j')$ are the effective neutron numbers for the pionic (nl) and neutron hole states ($n'l'j'$) listed in Table I. $F(E_x;c,g,s)$ is a Gaussian-folded Lorentzian function [19,20] whose center is c and whose width is g. The width of the folding Gaussian is s. Each Lorentzian corresponds to a configuration $(nl)_\pi(n'l'j')_n^{-1}$

Figure 2 schematically shows the fitting functions S_{1s} and S_{2p} for the pionic $1s$ and the $2p$ groups with the binding energies B_{1s} and B_{2p}, the widths Γ_{1s} and Γ_{2p}, the relative $1s$ and $2p$ intensities normalized to the theoretical prediction I_{1s} and I_{2p}, and the offset and the slope of the linear background c_0 and c_1, as free parameters. The centers of the Lorentzians are shown by the vertical lines. The height of each line represents the effective neutron number $N_{\rm eff}$ for the configuration shown in Table I. The width $\sigma_{\rm exp}$ of the folding Gaussian is the experimental resolution which was determined to be 0.48 ± 0.06 MeV (FWHM) [1].

Figure 3 presents the fit result. The experimental excitation spectrum is shown by the open circles with statistical error bars. The right edge of the fitting region is shown by the vertical dashed line, the best fit $1s$ and the $2p$ components by the dashed and the dotted curves, respectively, and the sum by the solid curve. The overall structure of the spectrum was fitted well and the χ^2 value was 115.2 ($N_{\rm DF}=120$). The obtained binding energies and widths with statistical errors were $B_{1s}=6.68\pm0.08$ MeV, $B_{2p}=5.13\pm0.02$ MeV, $\Gamma_{1s}=1.08\pm0.22$ MeV, and $\Gamma_{2p}=0.43\pm0.06$ MeV. The best-fit $1s/2p$ intensity ratio

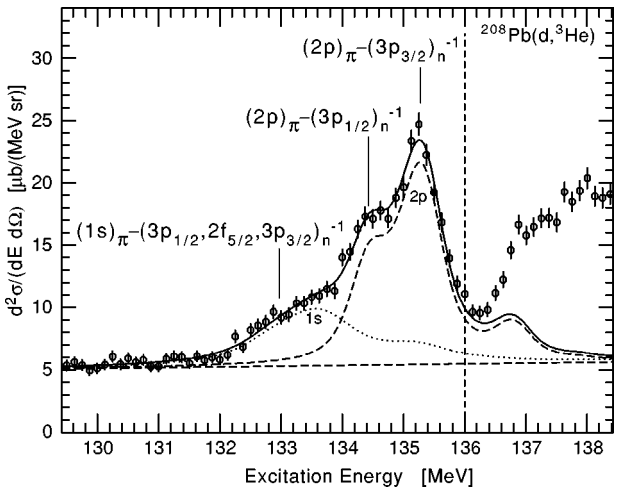

FIG. 3. The excitation spectrum obtained in the reaction ^{208}Pb(d,^{3}He) at $T_d=600$ MeV fitted by theoretical spectra of the $1s$ and $2p$ groups, respectively. The open circles show the experimental spectrum with statistical errors and the solid curve shows the fit result. The vertical dashed line shows the right edge of the fitting region. The tilted dashed line shows the linear background. The dotted and dashed curves show the $1s$ and $2p$ components, respectively.

$$R=[I_{1s}/I_{2p}], \tag{2.13}$$

was 1.63. The ratio R corresponds to an experimental $1s/2p$ cross section ratio divided by the theoretical $1s/2p$ cross section ratio, and thus the best-fit value 1.6 means that the relative $1s$ formation cross section to $2p$ was 60% larger than the theoretical one.

We examine the above fitting procedure in more details. Figures 4(a) and 4(b), respectively show the dependence of B_{2p} and B_{1s} on the choice of the intensity ratio R. The correlation between B_{2p} and R is not large, and the $2p$ binding energy and width are nearly unchanged by varying R. On the other hand, the B_{1s} indicates a strong correlation with R. This is simply because the $1s$ component is not observed as a separated peak but as a small bump sitting on the tail of the dominant $2p$ peak, and its fitting result is strongly affected by a slight change of the $2p$ shape. As the relative $1s$ intensity becomes smaller, the $1s$ component is pushed away towards larger binding energies. Moreover, B_{1s} and Γ_{1s} are also strongly correlated. From the theoretical side, it is not likely that ambiguities in the calculation can account for 60% discrepancy in the relative formation cross section of the $1s$ and $2p$ components. Thus, we cannot justify constraining value of R to 1.63 although it is the best-fit value, and we have to allow large uncertainties to B_{1s} and Γ_{1s}.

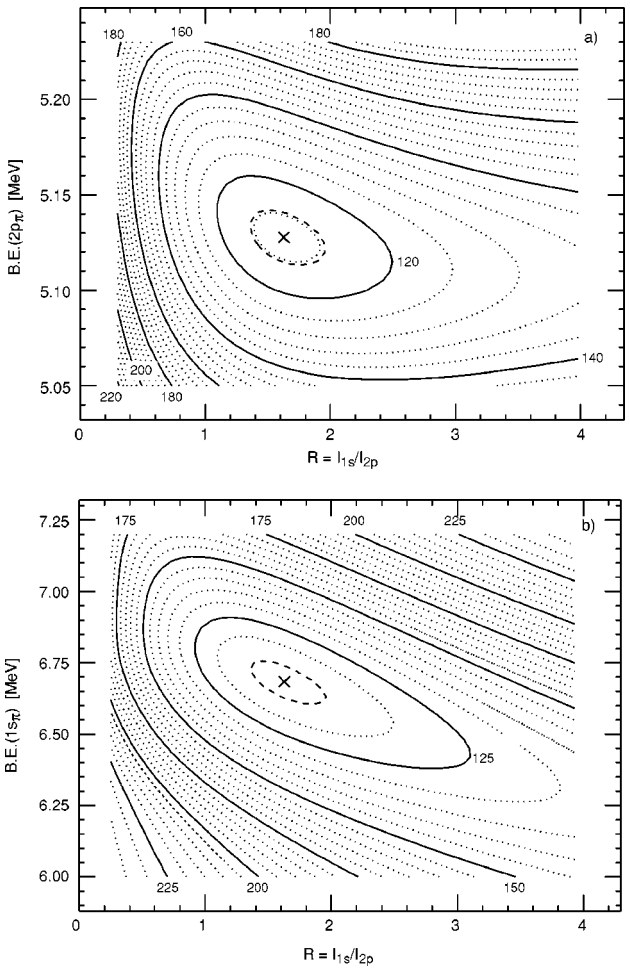

FIG. 4. Contour plots of χ^2 (a) in B_{2p} vs. I_{1s}/I_{2p} and (b) in B_{1s} vs. I_{1s}/I_{2p}. The dashed lines show 1-σ contours and the crosses χ^2 minima.

Systematic uncertainties of the fit for the $2p$ group were studied by performing fits under different conditions. (a) We observed that B_{2p} is hardly affected by varying the instrumental resolution $\sigma_{\rm exp}$. The Lorentzian width Γ_{2p} is changed by ± 0.06 MeV, as we allow an uncertainty of ∓ 0.06 MeV for $\sigma_{\rm exp}$. (b) There was no significant change in varying the fit range by ± 0.2 MeV. (c) We fitted the background region independently and found that a small variation of the background causes almost no change in B_{2p} and Γ_{2p}.

TABLE III. The obtained binding energy and width of 1s pionic sate and the fitting χ^2 are shown for four representative values of the intensity ratio R.

R		statistical	systematic		χ^2
1.63	$B_{1s}=6.68$	± 0.06	± 0.12	MeV	$115.2=\chi^2_{\rm min}$
	$\Gamma_{1s}=1.08$	± 0.13	± 0.06	MeV	
1.25	$B_{1s}=6.75$	± 0.06	± 0.12	MeV	117.3
	$\Gamma_{1s}=0.85$	± 0.12	± 0.06	MeV	
1.00	$B_{1s}=6.79$	± 0.06	± 0.12	MeV	122.3
	$\Gamma_{1s}=0.67$	± 0.11	± 0.06	MeV	
0.75	$B_{1s}=6.83$	± 0.06	± 0.12	MeV	132.3
	$\Gamma_{1s}=0.49$	± 0.11	± 0.06	MeV	

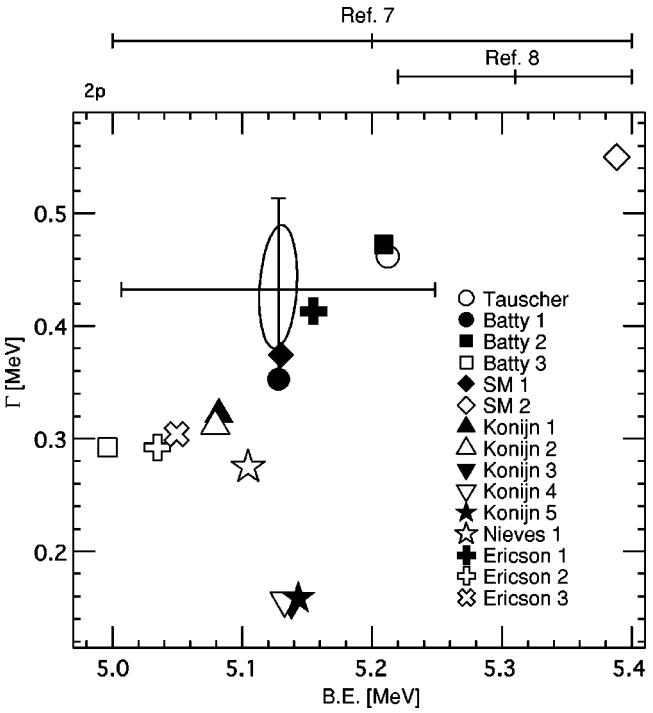

FIG. 5. A comparison of the obtained B_{2p} and Γ_{2p} with the existing theoretical values. The solid ellipse shows the statistical error (1-σ) and the bars show the systematic errors. Values of B_{2p} obtained at an earlier stage of the analysis, reported in Refs. [7] and [8], are compared at the top of the figure.

In conclusion, we have determined the binding energy and width of the $2p$ orbital as follows taking into accounts systematic errors in the absolute energy calibration (for B_{2p}) and in the experimental resolution (for Γ_{2p}),

$$B_{2p}=5.13\pm 0.02\,(\text{stat})\pm 0.12\,(\text{syst})\ \ \text{MeV},$$

$$\Gamma_{2p}=0.43\pm 0.06\,(\text{stat})\pm 0.06\,(\text{syst})\ \ \text{MeV}.$$

For 1s, we have obtained sets of B_{1s} and Γ_{1s} assuming several values of R, as shown in Table III.

III. COMPARISON OF B_{NL} AND Γ_{NL} WITH THEORETICAL CALCULATIONS

The binding energies and the widths of the pionic orbitals are theoretically obtained by solving the Klein-Gordon equation [Eq. (2.1)] numerically [21]. Here, we will compare our experimental results with the calculated values.

In the calculation we took the pion-nucleus optical potential parameters of Tauscher *et al.* [22], Batty *et al.* [23–25], Seki and Masutani [26] and Ericson *et al.* [27]. For parameters of Konijn *et al.* [28] and Nieves *et al.* [29] we adopted the values for the pion bound by ^{208}Pb from the references. The difference of the pionic state properties between ^{208}Pb and ^{207}Pb are small and were neglected. Table II shows the optical potential parameters and calculated B_{nl} and Γ_{nl}.

Figures 5 and 6 show two-dimensional plots of B_{nl} and

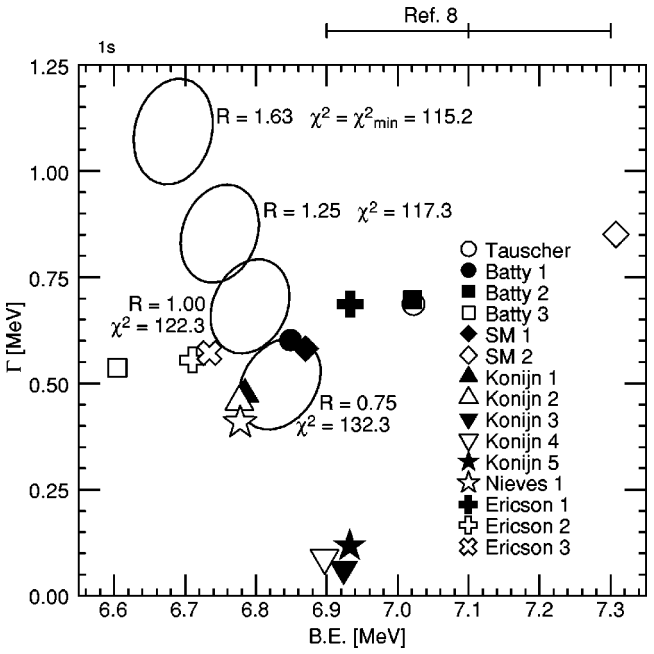

FIG. 6. A comparison of the obtained B_{1s} and Γ_{1s} with the existing theoretical values. The experimental results are shown by the ellipses ($1\text{-}\sigma$ contours) for various values of the intensity ratio ($R=1.50$, 1.25, 1.00, and 0.75). The fitting χ^2 for each intensity ratio is also shown ($N_{\mathrm{DF}}=119$). The value of B_{1s} obtained at an earlier stage of the analysis, given in Ref. [8], is compared at the top of the figure.

Γ_{nl} of the pionic $2p$ and $1s$ states, respectively. The experimental results obtained in the present alaysis and the theoretical values are presented together. The solid ellipses express the experimental values with statistical errors ($1-\sigma$). Quadratically added systematic errors are shown by the bars for the $2p$ state. For the $1s$ state, several ellipses are drawn for different values of the intensity ratio ($R=1.63$, 1.25, 1.00, and 0.75) labeled by the respectve χ^2 value of the fit. Values of B_{nl} obtained at an earlier stage of the analysis are plotted for comparison.

As seen in Fig. 5 for the $2p$ state, the present experimental result is precise enough to test the theoretical predictions, some of which overlap with our result within the error. Batty-1, 2, SM-1, Tauscher, and Ericson-1 are very close to the experimental values of both binding energy and width. Konijn-3-5 give narrower widths than the experiment, and SM-2 shows the largest deviation in the binding energy. These predictions are clearly disfavored by the experiment.

Figure 6 for the $1s$ state also provides some information. The ellipse for $R=1.63$ is far away from the theoretical predictions, and the ellipse for $R=1.0$ is near their central value. Konijn-3-5 give much too narrow widths again, and Batty-3 and SM-2 deviate from the binding energy allowed by the experiment.

IV. PION-NUCLEUS INTERACTION AND PION MASS SHIFT

A. Local potential strengths

Now we try to relate the binding energies and widths of the deeply bound states to the pion-nucleus potential parameters. So far, the nonlocal part (c_0, c_1, C_0, C_1) and the local imaginary part ($\mathrm{Im}\,B_0$) have been known rather well from pionic atom data. In shallow bound states the nonlocal parts play important roles, where the real part ($b_0, b_1\,\mathrm{Re}\,B_0$) of the s-wave (local) optical potential is only poorly known. On the other hand, the local part contributes dominantly to the observed strong interaction shifts

$$B_{1s}^{\mathrm{obs}}-B_{1s}^{\mathrm{Coulomb}}\simeq -5.3\mathrm{MeV}, \tag{4.1}$$

$$B_{2p}^{\mathrm{obs}}-B_{2p}^{\mathrm{Coulomb}}=-0.70\ \ \mathrm{MeV}, \tag{4.2}$$

where the pure-Coulomb values ($B_{nl}^{\mathrm{Coulomb}}$) for the $1s$ and $2p$ states are 12.06 MeV and 5.91 MeV, respectively. This situation is shown in Table IV.

TABLE IV. Contributions of the real local part, the real nonlocal part and the imaginary part of the strong interaction to the strong-interaction shifts of the pionic $1s$, $2p$, and $3d$ states in ^{207}Pb, calculated using the SM-1 parameter set. ''Real local'' denotes the binding energy shift due to the real local part of the optical potential from the value calculated with the finite size Coulomb potential. ''+ real nonlocal'' denotes the additional shift due to the real nonlocal part potential added, and ''+ imaginary'' the additional shift due to the imaginary part.

	ΔB_{1s} [MeV]	ΔB_{2p} [MeV]	ΔB_{3d} [MeV]
Real local	−5.302	−1.099	−0.061
+ real nonlocal	+0.136	+0.373	+0.103
+ imaginary	−0.027	−0.051	−0.009
Total	−5.194	−0.776	+0.032

Here, referring to the experimental results we tune the local-part potential parameters by adjusting their leading terms of the real (b_0) and the imaginary ($\mathrm{Im}\,B_0$) parts. In this analysis, we take four different potential parameter sets, Tauscher, Batty-2, SM-1, and Ericson-1 as the starting points, and change only b_0 and $\mathrm{Im}\,B_0$, while fixing the other parameters ($b_1, \mathrm{Re}\,B_0, c_0, c_1, C_0, C_1$) to the original values.

We express the real $[V(r)]$ and imaginary $[W(r)]$ parts of the local potential in the following forms:

$$U_{\mathrm{Local}}(r)=V(r)+iW(r) \tag{4.3}$$

with

$$V(r)=-\frac{2\pi}{\mu}[\epsilon_1\{b_0\rho(r)+b_1\Delta\rho(r)\}+\epsilon_2\,\mathrm{Re}\,B_0\rho^2(r)], \tag{4.4}$$

$$W(r)=-\frac{2\pi}{\mu}\epsilon_2\,\mathrm{Im}\,B_0\rho^2(r) \tag{4.5}$$

and relate them to B_{nl} and Γ_{nl}. We use the real strength $V(0)$ and the imaginary strength $W(0)$

$$V(0)=-455\left(b_0+\frac{N-Z}{A}b_1\right)-192\,\mathrm{Re}\,B_0\ \ \mathrm{MeV}, \tag{4.6}$$

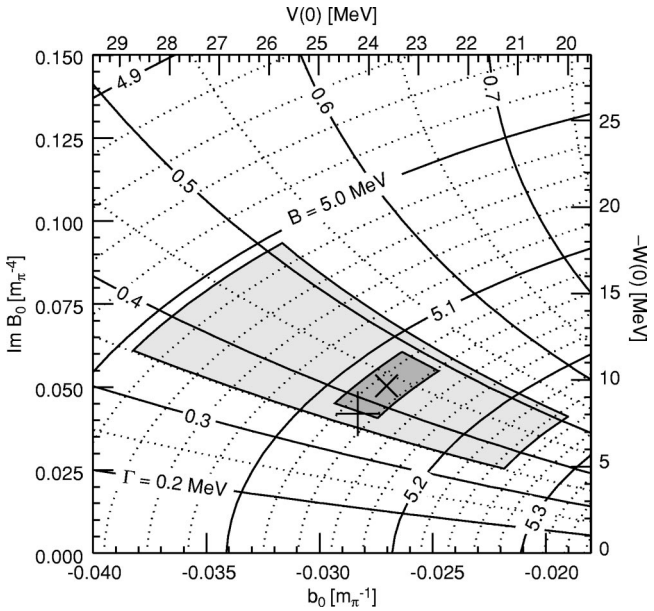

FIG. 7. The binding energy and width of the $2p\pi^-$ state are related to the real and imaginary local potential parameters b_0 and $\mathrm{Im}\,B_0$. The other parameters are fixed by the SM-1 parameter set. The parameters were converted to the potential depths at the center of the nucleus for the real part $V(0)$ and the imaginary part $W(0)$. The experimental value is shown by the tilted cross. The region allowed within the statistical error is shown by dark gray and that allowed within the systematic error in addition is shown by lighter gray. The original value of SM-1 parameter set is shown by the upright cross.

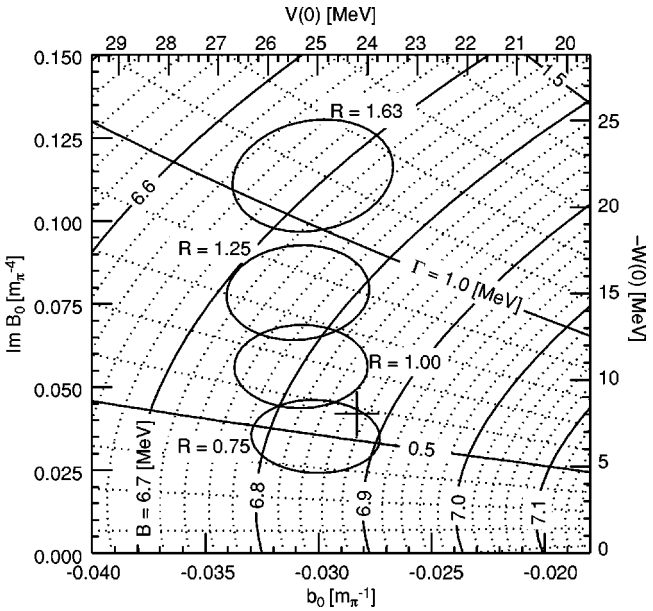

FIG. 8. The binding energy and width of the $1s\pi^-$ state are related to the real and imaginary local potential parameters b_0 and $\mathrm{Im}\,B_0$, and then to the potential depths $V(0)$ and $W(0)$ at the center of the nucleus. As in Fig. 7 the SM-1 parameter set is used for the other parameters. The experimental values are shown by 1-σ ellipses for labeled values of R. The original value given by the SM-1 parameter set is shown by the upright cross.

$$W(0) = -192\,\mathrm{Im}\,B_0 \quad \mathrm{MeV} \tag{4.7}$$

as representative parameters for the local potential.

In order to see the influence of the local potential, we calculate the binding energies and widths by varying $V(0)$ and $W(0)$. This was done by changing artificially b_0 and $\mathrm{Im}\,B_0$, while keeping the other parameters to the original values, as shown in Table II. The values of $[V(0),W(0)]$, (B_{1s},Γ_{1s}), and (B_{2p},Γ_{2p}) were calculated for each $(b_0,\mathrm{Im}\,B_0)$ value.

The calculated relations are presented for the case of the SM-1 parameter set in Fig. 7 for the $2p$ state and in Fig. 8 for the $1s$ state, respectively. The two figures are presented in the same scale for comparison. Basically, both B_{1s} and B_{2p} decrease with $V(0)$, but depend also on $W(0)$. As the imaginary part $[-W(0)]$ increases, it causes not only increase of the widths but also decrease of the binding energies. The widths also increase with the decrease of $V(0)$, as expected, because the halo character of the states becomes weaker as the repulsive barrier decreases.

The experimental results are shown by the tilted cross for the $2p$ state, and by $1-\sigma$ contours obtained in the previous fit for the $1s$ state with values of R as labeled. The statistical errors and the systematic errors in addition for B_{2p} and Γ_{2p} are shown by the regions with light and dark gray, respectively. The experimentally allowed zones in the $V(0)$-$W(0)$ plane for $2p$ (Fig. 7) and for $1s$ (Fig. 8) are different, but overlap partially, indicating the consistency between the results for the $1s$ state and for the $2p$ state within the current theoretical framework.

The local potential parameters $V(0)$ and $W(0)$ thus determined by using the experimental values of B_{2p} and Γ_{2p} are listed in Table V. They are different from the original values which are also shown in the table. The $V(0)$ values thus determined range from 23 to 27 MeV, reflecting the different parameter sets, while the $W(0)$ values are nearly the same. The parameters b_0 and $\mathrm{Im}\,B_0$ determined are also presented in the table.

In the above treatment we fixed $\mathrm{Re}\,B_0$ to the original values, which are model dependent. This is part of the reason for yielding different $V(0)$ values. If we allow $\mathrm{Re}\,B_0$ to be varied, we have to change the $V(0)$ value accordingly. However the two parameters, b_0 and $\mathrm{Re}\,B_0$, are interrelated as in the Seki-Masutani relation obtained by reading from Fig. 1 in Ref. [26],

$$b_0\rho(0) + 0.50\times \mathrm{Re}\,B_0\rho^2(0) = 0.062 \quad \mathrm{fm}^{-2}. \tag{4.8}$$

This relation can be derived by asserting that the binding energies are determined essentially by the local potential strength at the nuclear radius ($r=R_0$). Since $\rho(R_0) = (1/2)\rho(0)$, this means b_0 and $\mathrm{Re}\,B_0$ satisfy the relation

$$\text{assertion:}\quad V(R_0) = -\frac{2\pi}{\mu}\left[\frac{1}{2}\epsilon_1[b_0\rho(0) + b_1\Delta\rho(0)] + \frac{1}{4}\epsilon_2\,\mathrm{Re}\,B_0\rho(0)^2\right] \sim \mathrm{const.} \tag{4.9}$$

TABLE V. Real $V(0)$ and imaginary $W(0)$ strengths of the local potential deduced from the experimental results on the $2p$ state based on four models which use different potential parameter sets. The corresponding values of b_0 and $\mathrm{Im}\,B_0$ parameters are also shown. The original values of $V(0)$ and $W(0)$ are presented for comparison. The $V(R_0)$ values determined are also shown. The errors are chosen to cover the experimental errors.

Model	$V(0)_{\mathrm{brig}}$	$-W(0)_{\mathrm{brig}}$	$V(0)_{\mathrm{det}}$	$-W(0)_{\mathrm{det}}$	b_0	$\mathrm{Im}\,B_0$	$\mathrm{Re}\,B_0$	$2V(R_0)_{\mathrm{det}}$
Tauscher	20.7	8.2	$23.0^{+5.0}_{-3.6}$	$10.0^{+8.1}_{-4.8}$	$-0.034^{+0.008}_{-0.011}$	$0.052^{+0.042}_{-0.025}$	0	23.0
Batty-2	22.5	9.4	$23.3^{+4.8}_{-3.5}$	$8.9^{+7.2}_{-4.4}$	$-0.025^{+0.008}_{-0.011}$	$0.046^{+0.038}_{-0.023}$	-0.021	21.3
SM-1	24.2	8.1	$23.6^{+5.1}_{-3.6}$	$9.7^{+8.2}_{-4.8}$	$-0.027^{+0.008}_{-0.011}$	$0.050^{+0.043}_{-0.025}$	0	23.6
Ericson-1	26.3	9.4	$26.9^{+5.3}_{-3.9}$	$10.8^{+8.5}_{-5.1}$	$-0.020^{+0.009}_{-0.012}$	$0.056^{+0.044}_{-0.027}$	-0.049	22.2

Thus, each term cannot be uniquely determined. The above relation is nearly the same as the Seki-Masutani relation (4.8).

The validity of the above assertion is illustrated in Fig. 9, where the two different potentials (solid and dashed curves) that have the same value at $r=R_0$ are shown to give nearly the same binding energies ($\Delta B_{1s}\sim 0.07$ MeV) and nearly the same π^- density distributions. $V(R_0)$ is a more invariant quantity than $V(0)$ to describe the binding energies of the deeply bound π^- states. The notch test proposed in Ref. [23] is in accordance with the spirit of the above assertion.

Thus, the local potential strength $V(0)$ is related to $V(R_0)$ as

$$2V(R_0)=V(0)+\frac{2\pi}{\mu}\frac{1}{2}\epsilon_2\,\mathrm{Re}\,B_0\rho(0)^2$$
$$=V(0)+85\,\mathrm{Re}\,B_0\ \ \mathrm{MeV}. \tag{4.10}$$

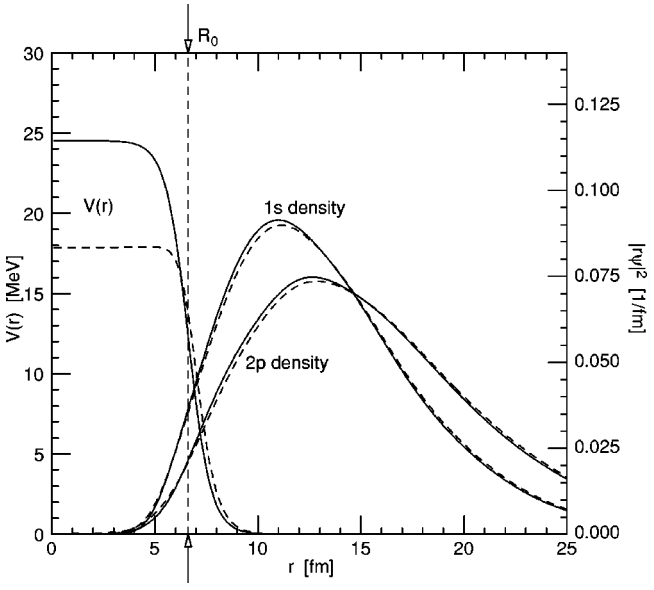

FIG. 9. Two different real local-part potentials which give nearly the same binding energies, widths, and π^- densities. The solid and dashed curves were calculated with $(b_0,\mathrm{Re}\,B_0)=(-0.0283,0.0)$ (=original SM-1) and $(-0.0561,\ 0.1)$, respectively. The calculations were done for ^{207}Pb by fixing the other parameters to the original values of the SM-1 parameter set shown in Table II. The half density radius is shown by the arrows and the vertical dashed line.

The values of $2V(R_0)$ calculated from the determined values of $V(0)$ are also presented in Table V. They are in the region 21–23 MeV, demonstrating the validity of the above assertion. It is remarkable that all the different starting potential parameters converge into the common value of $2V(R_0)$ to account for the experimental B_{2p} and Γ_{2p}. This result justifies the present prescription. Although B_{1s} is most sensitive to $V(0)$, its experimental value from the present experiment has a larger uncertainty, and the corresponding constraint on $V(0)$ is weaker, though the above two independent values from $1s$ and $2p$ are mutually consistent.

B. Effective pion mass

The local potential thus determined can be translated into an effective mass of π^- in ^{207}Pb [8]. For an infinite system of nuclear density ρ, the effective pion mass $m_\pi^{\mathrm{eff}}(\rho)$ is defined as the real part of the self energy for a pion at rest ($\vec{q}=0$) in matter [30]

$$[m_\pi^{\mathrm{eff}}(\rho)]^2=[m_\pi^2+\vec{q}^{\,2}+\mathrm{Re}\,\Pi(E,\vec{q};\rho)]_{\vec{q}\to 0}\sim m_\pi^2+2m_\pi V(r), \tag{4.11}$$

since the nonlocal (p-wave) part vanishes as $\vec{q}\to 0$. This yields

$$m_\pi^{\mathrm{eff}}(r)\sim m_\pi+\Delta m_\pi^{\mathrm{eff}}(r), \tag{4.12}$$

where

$$\Delta m_\pi^{\mathrm{eff}}(r)=V(r). \tag{4.13}$$

Namely, the pion mass shift $\Delta m_\pi^{\mathrm{eff}}(r)$ is equal to the real part of the s-wave potential $V(r)$. So, we conclude that the π^- mass at the center of the ^{207}Pb nucleus increases by

$$\Delta m_\pi^{\mathrm{eff}}(0)=23\sim 27\ \ \mathrm{MeV}, \tag{4.14}$$

allowing the uncertainty in $\mathrm{Re}\,B_0$. The obtained radial dependence of $\Delta m_\pi^{\mathrm{eff}}(r)$ assuming the SM-1 parameter set is shown in Fig. 10. The above result is consistent with the calculated mass shift of about 21 MeV at the center of Pb nucleus [30] obtained from low-energy theorems based on the chiral symmetry of QCD [31,32].

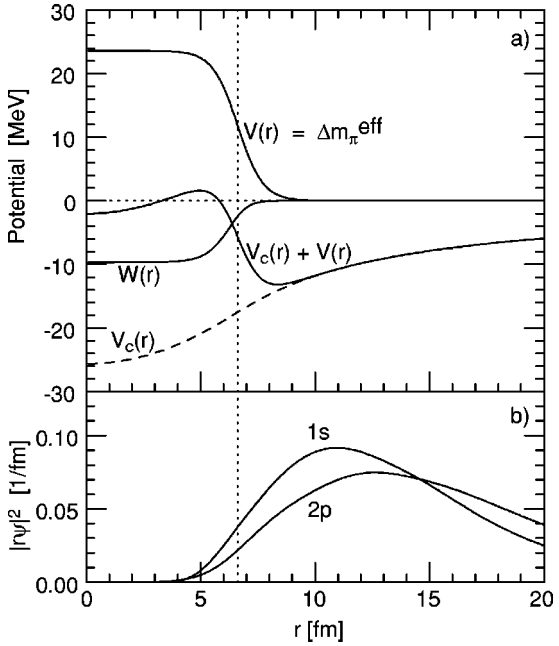

FIG. 10. (a) The real part of local potential $V(r)$, which is equivalent to the pion mass shift $\Delta m_\pi^{\rm eff}(r)$, the total real-part potential including the Coulomb interaction $(V_c(r))$, and the imaginary part of the local potential $(W(r))$, as obtained from the analysis of the measured $1s$ and $2p\pi^-$ binding energies and widths based on the SM-1 parameter set. Re B_0 was not changed in the analysis. (b) Radial distributions of the $1s$ and $2p\pi^-$ densities. The half density radius is shown by the vertical dotted line.

V. CONCLUDING REMARKS

In the Ericson-Ericson type formulation of the pion-nucleus optical potential the *p*-wave (nonlocal) part parameters have relatively strict restrictions from existing data, while the *s*-wave (local) part parameters have had larger uncertainties so far. Sensitivity of a pionic state to this *s*-wave part parameters is proportional to the overlap integral between the pionic density and the nuclear medium $[\int|\psi_\pi(r)|^2\rho(r)dr^3]$, and thus, the $1s$ and $2p$ pionic states in heavy nuclei are the most suitable for the study of the *s*-wave parameters.

Since such deeply bound states could not be formed in the conventional method of using stopped pions [33], we developed pion-transfer reactions [3]. Several experiments were tried by using (n,p) [34], (n,d) [35,36], $(d,{}^2\mathrm{He})$ [37], $(d,{}^3\mathrm{He})$ [38], $(p,2p)$ [39] reactions, resulting in no clear evidence of pionic atom formation. In the meantime, the theoretical investigation was continued to find the optimal experimental condition. Finally, the $(d,{}^3\mathrm{He})$ reaction was found to be suitable in producing pionic states under the recoilless condition $(\Delta q\sim 0)$. This condition was expected to enhance the cross section for the formation of a bound pionic state of substitutional configuration $(l_{\pi^-}=l_n)$.

This new method involved several questions. (i) Can the optical potential deduced from shallow pionic atoms be applied to deeply bound states? (ii) Are the calculated production cross sections correct? (iii) Is the intrinsic background small enough to observe the bound-pion peaks? (iv) Can the instrumental background be suppressed sufficiently? (v) Is the energy resolution good enough?

The present experimental setup was carefully designed based on the previous experiences. It was optimized to achieve the highest possible resolution at sufficiently high yield and low background. In the design of the experiment, the fragment separator (FRS) [40] at the GSI was a key component. It was used as a spectrometer at forward 0°, and its two 30° dipole magnets after the target bending in opposite directions swept out most of the background particles before they reach the dispersive focal plane. The second part of the FRS worked as a 36 m long transfer line, where the particles were perfectly identified by the time of flight and by the energy loss in the scintillation counters. The synchrotron SIS-18 provided a high intensity beam$>10^{11}$ d/spill, with a small momentum spread $\Delta p/p<5\times10^{-4}$, which corresponds to an energy resolution <0.3 MeV. The experimental resolution and the symmetric spectral response were guaranteed by the monoenergetic peak of ^{3}He from the two-body reaction of $p(d,{}^3\mathrm{He})\pi^0$ by using a polyethylene $[(\mathrm{CH}_2)_n]$ target.

The finally obtained energy spectrum after careful corrections for the acceptance of the spectrometer, the target thickness, the time dependent incident beam momentum drift within the extraction, second order ion optical aberrations, and other contributions had a resolution of 0.48 ±0.06 MeV, and was in notable agreement with the theoretically calculated spectrum in the whole measured range.

The observed absolute cross sections are found to be by a factor of 2.5 smaller than the theoretical values, which is within the uncertainty of the calculation of absolute cross sections. There was a prominent peak at about 5 MeV below the π^- production threshold, and it was assigned to the formation of the $2p$ pionic state coupled to neutron hole states of $3p_{1/2}$ and $3p_{3/2}$, which are separated by 0.9 MeV. Structure due to the formation of shallower states was also seen between the $2p$ peak and the threshold. An additional peak, though unresolved, was observed in the $(1s)_{\pi^-}$ region and was assigned to the configurations of $(1s)_{\pi^-}(3p_{1/2},2f_{5/2},3p_{3/2})_n^{-1}$.

We analyzed the excitation spectrum of $^{208}\mathrm{Pb}(d,{}^3\mathrm{He})$ reaction in terms of the formation of bound pionic states in the nuclear reaction, and deduced the binding energy and the width of the $2p$ state to be $B_{2p}=5.13\pm0.02\,(\mathrm{stat})\pm0.12\,(\mathrm{syst})$ MeV, $\Gamma_{2p}=0.43\pm0.06\,(\mathrm{stat})\pm0.06\,(\mathrm{syst})$ MeV. The formation of the $1s$ ground state was clearly observed, but the precise determination of the binding energy and width was not possible because of the incomplete separation from the main peak. Constraints of B_{1s} vs Γ_{1s} were presented for each of assumed $1s/2p$ cross section ratios as listed in Table III.

The binding energies and widths are compared with the calculated values using the existing potential parameter sets. The resolution was high enough to test the validity of the model predictions. In their relation to the theoretically calculated values, the deduced values of $1s$ and $2p$ states are in mutual accordance. The widths expected from Konijn *et al.* [28] in which the potential parameters were adjusted to fit to the data showing the $3d$ anomaly [9,10,41] were smaller

than the experimental results by more than three standard deviations. The experimental values were closer to those expected from older parameter sets developed before the $3d$ anomaly was introduced, as shown in Figs. 5 and 6.

For the deeply bound π^- states the binding energies and widths depend predominantly on the real and imaginary parts of the local potential, $V(r)$ and $W(r)$, respectively. Therefore, we calculated the binding energy and width for each state in the $V(r)-W(r)$ plane, and presented the experimentally allowed region. We took four different potential parameter sets and determined $V(r)$ and $W(r)$ experimentally. We demonstrated that the real local potential strength $V(R_0)$ at the nuclear radius ($r=R_0$) is nearly independent of the assumed initial parameter sets. In this way we have proved the assertion that the binding energies and widths are determined by the potential strengths at $r=R_0$. This means that b_0 and $\mathrm{Re}\,B_0$ cannot be determined separately, but follow the Seki-Masutani type relation.

The obtained local potential strength indicated that the pion mass at the center of ^{207}Pb nucleus is 23–27 MeV larger than in vacuum, though there still remains a small uncertainty originating from $\mathrm{Re}\,B_0$ [42]. The deeply bound pionic states can also be recognized as a kind of Gamow-Teller resonances ($\Delta S=\Delta I=1$), which are located at an excitation energy of about 135 MeV in ^{207}Pb [43]. Another remarkable conclusion is that the structureless background of about 5 μb/(MeV sr) observed in the region $120\,\mathrm{MeV}<E_x<130\,\mathrm{MeV}$ is not an instrumental background but a genuine physical continuum due to processes with high nuclear excitation energies without pion production. This cross section was 60 times smaller than the one [300 μb/(MeV sr)] observed in the $^{208}\mathrm{Pb}(n,d)$ reaction at 400 MeV [35].

Our goal in the near future is to observe the $1s$ state as a separated peak. In the present spectrum, the $1s$ component is obscured by the shoulderlike structure of $(2p)_\pi(3p_{1/2})_n^{-1}$ [$(3p_{1/2})_n^{-1}$ = ground state of ^{207}Pb]. In a forthcoming experiment, we plan to use ^{206}Pb instead of ^{208}Pb to get rid of this obstructive contribution from the $3p_{1/2}$ neutron hole according to the theoretical investigations [44], and expect to determine the B_{1s} and Γ_{1s} with higher precision.

Recent theoretical studies on chiral symmetry breaking in QCD show that hadron properties in nuclei are closely related to the magnitude of the chiral quark condensate at finite nuclear density and related to the non-trivial structure of the QCD vacuum [45–47]. In this context, there is currently a lot of interest in the investigation of hadron properties in nuclear matter. The present discovery of pionic atom formation in nuclear reactions simultaneously accomplished the method of populating a mesic bound state in nucleus, which can be widely applied to the deduction of the meson's effective mass in the medium. This method has a unique merit compared with the invariant mass spectroscopy as applied to decaying mesons in nuclei [48–53], as the latter method suffers from the final state interactions (collisional decays) [54]. Experimental investigation based on a theoretical study [55] of the production of η- and ω-mesic nuclei is under way [56].

ACKNOWLEDGMENTS

The authors thank Y. Umemoto for fruitful discussion and valuable comments. One of the authors (K.I.) acknowledges the Japan Society for the Promotion of Science. This work was supported by the Grant-in-Aid for Scientific Research of Monbusho (Japan) and by the Bundesministerium für Bildung, Wissenschaft, Forschung und Technologie (Germany).

[1] H. Gilg, A. Gillitzer, M. Knülle, M. Münch, W. Schott, P. Kienle, K. Itahashi, K. Oyama, R. S. Hayano, H. Geissel, N. Iwasa, G. Münzenberg, and T. Yamazaki, Phys. Rev. C **62**, 025201 (2000), preceding paper.
[2] E. Friedman and G. Soff, J. Phys. G **11**, L37 (1985).
[3] H. Toki and T. Yamazaki, Phys. Lett. B **213**, 129 (1988).
[4] H. Toki, S. Hirenzaki, T. Yamazaki, and R. S. Hayano, Nucl. Phys. **A501**, 653 (1989).
[5] H. Toki, S. Hirenzaki, and T. Yamazaki, Nucl. Phys. **A530**, 679 (1991).
[6] S. Hirenzaki, H. Toki, and T. Yamazaki, Phys. Rev. C **44**, 2472 (1991).
[7] T. Yamazaki, R. S. Hayano, K. Itahashi, K. Oyama, A. Gillitzer, H. Gilg, M. Knülle, M. Münch, P. Kienle, W. Schott, H. Geissel, N. Iwasa, and G. Münzenberg, Z. Phys. A **355**, 219 (1996).
[8] T. Yamazaki, R. S. Hayano, K. Itahashi, K. Oyama, A. Gillitzer, H. Gilg, M. Knülle, M. Münch, P. Kienle, W. Schott, W. Weise, H. Geissel, N. Iwasa, G. Münzenberg, S. Hirenzaki, and H. Toki, Phys. Lett. B **418**, 246 (1998).
[9] A. Olin, J. W. Forsman, J. A. Macdonald, G. M. Marshall, T. Numao, G. A. Beer, D. I. Britton, G. R. Mason, A. R. Kunselman, and B. H. Olaniyi, Nucl. Phys. **A439**, 589 (1985).
[10] C. T. A. M. De Laat, A. Taal, J. Konijn, P. David, H. Hänscheid, F. Risse, Ch. Rösel, and W. Wchrieder, Nucl. Phys. **A523**, 453 (1991).
[11] H. de Vries, C. W. de Jager, and C. de Vries, At. Data Nucl. Data Tables **36**, 495 (1987).
[12] L. S. Kisslinger, Phys. Rev. **98**, 761 (1955).
[13] M. Ericson and T. E. O. Ericson, Ann. Phys. (N.Y.) **36**, 323 (1966).
[14] C. B. Dover, L. Ludeking, and G. E. Walker, Phys. Rev. C **22**, 2073 (1980).
[15] S. Hirenzaki and H. Toki, Nucl. Phys. **A628**, 403 (1998).
[16] Paritcle data group, Eur. Phys. J. C **3**, 1 (1998).
[17] H. W. Fearing, Phys. Rev. C **16**, 313 (1977).
[18] M. Matoba, K. Yamaguchi, K. Kurohmaru, O. Iwamoto, Susilo Widodo, A. Nohtomi, Y. Uozumi, T. Sakae, N. Koori, T. Maki, and M. Nakano, Phys. Rev. C **55**, 3152 (1997).
[19] B. L. Roberts, R. A. J. Riddle, and G. T. A. Squier, Nucl. Instrum. Methods **130**, 559 (1975).
[20] C. J. Batty, S. D. Hoath, and B. L. Roberts, Nucl. Instrum. Methods **137**, 179 (1976).
[21] Y. R. Kwon and F. Tabakin, Phys. Rev. C **18**, 932 (1978).
[22] L. Tauscher in Proceedings of the International Seminar on π-Meson Nucleus Interaction Strasbourg 1971, CNRS-

Strasbourg (unpublished), p. 45.
[23] C. J. Batty, E. Friedman, and A. Gal, Phys. Rep. **287**, 385 (1997).
[24] C. J. Batty, S. F. Biagi, E. Friedman, S. Hoath, J. D. Davies, G. J. Pyle, G. T. A. Squier, D. M. Asbury, and A. Guberman, Nucl. Phys. **A322**, 445 (1979); C. J. Batty, S. F. Biagi, E. Friedman, S. Hoath, J. D. Davies, G. J. Pyle, and G. T. A. Squier, Phys. Rev. Lett. **40**, 931 (1978).
[25] C. J. Batty, E. Friedman, and A. Gal, Nucl. Phys. **A402**, 411 (1983).
[26] R. Seki and K. Masutani, Phys. Rev. C **27**, 2799 (1983).
[27] T. E. O. Ericson and L. Tauscher, Phys. Lett. **112B**, 425 (1982).
[28] J. Konijn, C. T. A. M. De Laat, A. Taal, and J. H. Koch, Nucl. Phys. **A519**, 773 (1990).
[29] J. Nieves, E. Oset, and C. Garcia-Recio, Nucl. Phys. **A554**, 509 (1993).
[30] T. Waas, R. Brockmann, and W. Weise, Phys. Lett. B **405**, 215 (1997).
[31] Y. Tomozawa, Nuovo Cimento A **46**, 707 (1966).
[32] S. Weinberg, Phys. Rev. Lett. **17**, 616 (1966).
[33] G. Backenstoss, Annu. Rev. Nucl. Sci. **20**, 467 (1970).
[34] M. Iwasaki *et al.*, Phys. Rev. C **43**, 1099 (1991).
[35] A. Trudel *et al.*, TRIUMF Progress report, 1991.
[36] T. Yamazaki, Phys. Scr. **48**, 169 (1993).
[37] T. Yamazaki *et al.*, Saturne Proposal No. 214, 1988 (unpublished).
[38] T. Yamazaki, R. S. Hayano, H. Toki, and H. Langevin-Joliot, Saturne Proposal No. 254, 1992 (unpublished).
[39] N. Matsuoka, T. Noro, K. Tamura, M. Yoshimura, M. Yosoi, A. Okihana, and T. Yoshimura, Phys. Lett. B **359**, 39 (1995).
[40] H. Geissel *et al.*, Nucl. Instrum. Methods Phys. Res. B **70**, 286 (1992).
[41] J. Konijn, J. K. Panman, J. H. Koch, W. van Doesburg, G. T. Ewan, T. Johansson, G. Tibell, K. Fransson, and L. Tauscher, Nucl. Phys. **A326**, 401 (1979).
[42] E. Friedman and A. Gal, Phys. Lett. B **432**, 235 (1998).
[43] T. Yamazaki, in *New Facet of Spin Giant Resonances in Nuclei*, edited by H. Sakai, H. Okamura, and T. Wakasa (World Scientific, Singapore, 1998), p. 357.
[44] S. Hirenzaki and H. Toki, Phys. Rev. C **55**, 2719 (1997).
[45] T. Hatsuda and T. Kunihiro, Prog. Theor. Phys. **74**, 765 (1985); Phys. Rep. **247**, 221 (1994).
[46] G. E. Brown and M. Rho, Phys. Rep. **269**, 333 (1996); Y. Nambu, in *Festschrift for Val Telegdi*, edited by K. Winter (Elsevier Scientific Publisher, New York, 1988), p. 181.
[47] U. Vogl and W. Weise, Prog. Part. Nucl. Phys. **27**, 195 (1991).
[48] Y. Akiba *et al.*, Phenix Collaboration, Nucl. Phys. **A638**, 565c (1998).
[49] The Hades Collaboration, GSI scientific report 1996 (unpublished), p. 193.
[50] G. Agakichiev *et al.*, CERES Collaboration, Phys. Rev. Lett. **75**, 1272 (1995).
[51] Th. Ullrich *et al.*, CERES Collaboration, Nucl. Phys. **A610**, 317c (1996).
[52] M. Masera, HELIOS Collaboration, Nucl. Phys. **A590**, 93c (1995).
[53] K. Maruyama, Nucl. Phys. **A629**, 351c (1998).
[54] T. Yamazaki and Y. Akaishi, Phys. Lett. B **453**, 1 (1999).
[55] R. S. Hayano, S. Hirenzaki, and A. Gillitzer, Eur. Phys. J. A **6**, 99 (1999).
[56] S214, Experimental Proposal for GSI/SIS, 1997 (unpublished).
[57] L. Tauscher and W. Schneider, Z. Phys. **271**, 409 (1974).
[58] J. Hüfner, Nucl. Phys. **B58**, 55 (1973).
[59] E. J. Moniz, I. Sick, R. R. Whitney, J. R. Ficenec, R. D. Kephart, and W. P. Trower, Phys. Rev. Lett. **25**, 445 (1971).